Electronic Supplementary Material (ESI) for Journal of Materials Chemistry A.

Boosting CH_4 selectivity in CO_2 electroreduction by a metallacycle-based porous crystal with biomimetic adaptive cavities

Xin Wang[#a], Zhi-Wei Li*[#a], Zi-Jun Huang[a], Li-Ping Li[a], Xiao-Ru Peng[a], Mei-Jie Shang[ab], Pei-Sen Liao[a], Hsiu-Yi Chao[a], Gangfeng Ouyang[a], and Gao-Feng Liu*[a]

[a]MOE Key Laboratory of Bioinorganic and Synthetic Chemistry, School of Chemistry, Sun Yat-Sen University, Guangzhou 510275, China.

[b]Electric Power Research Institute of Guangxi Power Grid Co., Ltd., Guangxi Nanning 530000, China

[#]X.W. and Z.W.L. contributed equally to this work.

*E-mail: lizhw69@mail.sysu.edu.cn ; liugaof@mail.sysu.edu.cn

1. Material synthesis and Characterization

Chemicals.

All starting regents and chemicals were commercially available and used as received without further purification. The deionized water used throughout all experiments was supplied with a Milli-Q ultrapure water system (18.2 MΩ·cm).

Characterization.

Nuclear magnetic resonance spectra (^{1}H NMR and ^{13}C NMR) images were obtained using a Bruker Ascend 400 MHz spectrometers. Chemical shifts are reported as ppm. Date for ^{1}H NMR spectra are referred to the internal reference TMS signal and ^{13}C NMR spectra are referred to the residual solvent signal.

Low resolution mass spectra of subcomponents were carried out on Thermo Fisher Scientific LTQ XL. High resolution electrospray ionization mass spectrometry (HR-ESI) experiments were measured with a Waters Synapt G2-Si Ion Mobility-Q-TOF High Resolution LC-MS instrument.

The elemental analyses of C, H and N were performed on a PerkinElmer 240 elemental analyzer.

IR spectra were recorded in the range of 4000-450 cm^{-1} on a Bruker FT-IR spectrometer (EQUINOX 55) using the KBr disc technique. UV-Vis spectra were recorded on a Shimadzu UV-3600 spectrometer.

Thermogravimetric analysis (TGA) were performed on a NETZSCH TG209 system under N_2 atmosphere in the range of 30-800 °C at a heating rate of 10 °C·min^{-1}. The thermogravimetric-differential thermal analysis (TG-DTA) were recorded on a Thermo plus EV2 instrument, and TG-MS measurements were measured by a Thermo mass photo system.

Powder X-ray diffraction (PXRD) data were recorded on a Bruker D8 powder X-ray diffractometer with Cu *Kα* radiation (λ = 1.5406 Å). Variable-temperature powder X-ray diffraction (VT-PXRD) patterns were collected under N_2 atmosphere in the range of 30-260 °C with a heating rate of 10 °C·min^{-1}, sampling interval is 20 °C.

N_2 adsorption measurements were measured using a Micromertics ASAP 2460 instrument. The CO_2 isotherms were measured with an automatic volumetric sorption apparatus Micromertics ASAP 2020.

Before sorption experiments, the sample was heated at 150 °C under high vacuum for 12 hours to remove the remnant solvent molecules.

Scanning electron microscopy (SEM) were taken on a FE-SEM (SU8010) working at 10 kV.

X-ray photoelectron spectrometer (XPS) measurements were performed on an ESCALAB 250Xi X-ray photoelectron spectrometer (Thermo Fisher).

XAFS spectra at Cu *K*-edge were measured at beamline XDD station of the Singapore Synchrotron Light Source, Singapore.

The *in situ* PXRD/adsorption measurements were carried out using a Rigaku SmartLab PXRD instrument with Cu-K*a* radiation connected to MicrotracBEL Max adsorption equipment, which were synchronized with each other, and each PXRD pattern was started to scan (0.02/step and 8/min) just after each isotherm data point was recorded.

Calculation of isosteric heat of adsorption (Q_{st}). Virial fitting equation:

$$\ln\ p = \ln\ n + \frac{1}{T}\sum_{i=0}^{l} a_i n^i + \sum_{j=0}^{m} b_j n^i$$

where p is pressure, n is amount adsorbed, T is temperature, and a_i and b_j are temperature independent empirical parameters.

The isosteric heat of adsorption was calculated with the Virial equation[S1] using CO_2 isotherms measured at 273 and 298 K:

$$Q_{st} = -R\sum_{i=o}^{l} a_i n^i$$

where R is the universal gas constant, 8.314 J·mol^{-1}·K^{-1}.

Single-Crystal X-ray Crystallography. The diffraction data of **1·CH$_3$CN** was collected on an Oxford Xcalibur, Sapphire3, Gemini ultra CCD diffractometer equipped with monochromatic Cu *K*α radiation (λ = 1.54184 Å) at 198(20) K. The diffraction data of **1·C$_6$H$_6$** was collect on an Agilent Sapphire3 Gemini Ultra single crystal diffractometer using Cu radiation (λ = 1.54184 Å) at 150.01(12) K. The intensity data were corrected for Lorentz and polarization effects (SAINT), and empirical absorption corrections based on equivalent reflections were applied (SADABS)[S2]. The structures were solved by direct methods and

refined by the full-matrix least-squares method on F^2 with SHELXTL program package[S3]. All non-hydrogen atoms were refined with anisotropic displacement parameters. The hydrogen atoms were calculated and refined as a riding model.

2. Synthesis of H_4L.

Scheme S1. Synthetic scheme for **H_4L**.

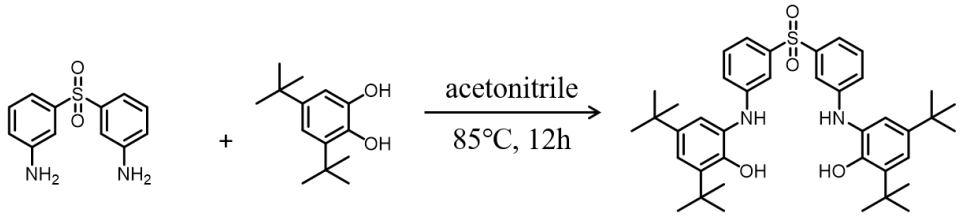

1,1-di-(3-(2-hydroxy-3,5-di-tert-butyl)phenyl)amino)phenyl-sulfone (**H_4L**) was synthesized using modified literature procedure.[S4] In a 25 mL round-bottomed flask, 3,5-di-tert-butylcatechol (444.0 mg, 2.0 mmol) and 3,3'-diaminodiphenyl sulfone (248.0 mg, 1.0 mmol) were dissolved in 10 mL acetonitrile and refluxed for 12 hours. After cooling down to room temperature, the reaction mixture was poured into n-hexane. The precipitated product was filtered and washed with cold acetonitrile to yield a light red solid (600.0 mg, 91.6%). ^{1}H NMR (400 MHz, DMSO-d_6) δ = 8.11 (s, 1H), 7.75 (s, 1H), 7.30 (t, *J* = 7.7 Hz, 1H), 7.18 (s, 1H), 7.07 (d, *J* = 7.7 Hz, 1H), 7.04 (s, 1H), 6.96 (s, 1H), 6.85 (d, *J* = 8.1 Hz, 1H), 1.38 (s, 9H), 1.21 (s, 9H). ^{13}C NMR (101 MHz, DMSO-d_6) δ 148.14, 147.98, 142.29, 141.34, 137.01, 130.38, 128.80, 119.86, 119.66, 118.90, 115.86, 111.96, 39.99, 39.78, 35.22, 34.38, 31.87, 30.05. ESI-MS (m/z): calcd. for [**H_3L**]$^-$, 655.36. Found: [**H_4L-H**]$^-$, 655.55.

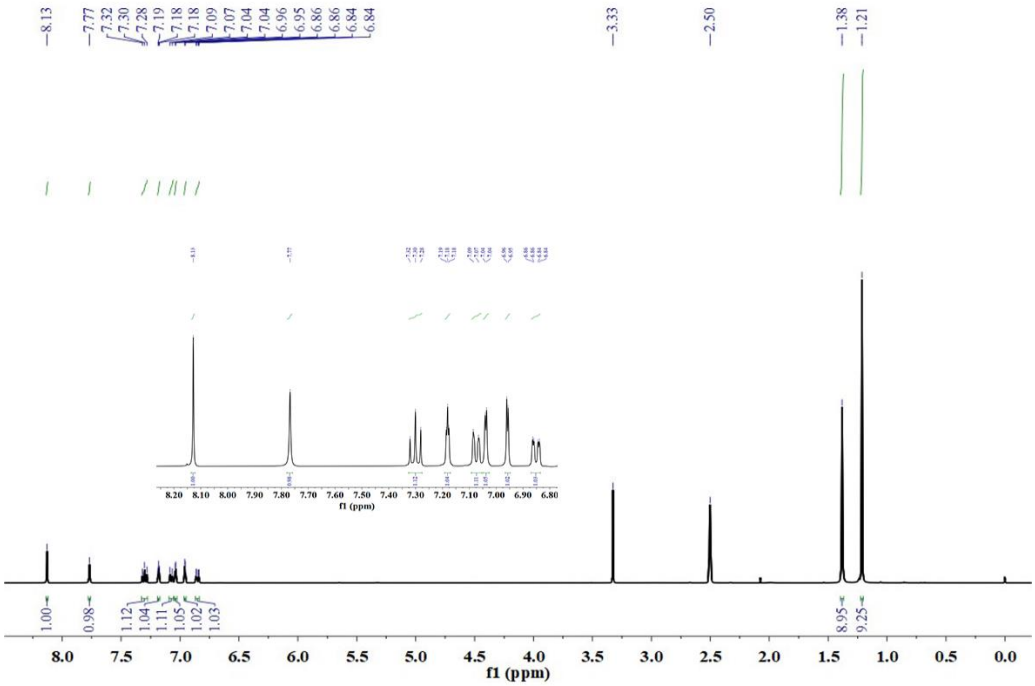

Figure S1. ^{1}H NMR spectrum of **H_4L** (400 MHz, DMSO-d_6, 298 K).

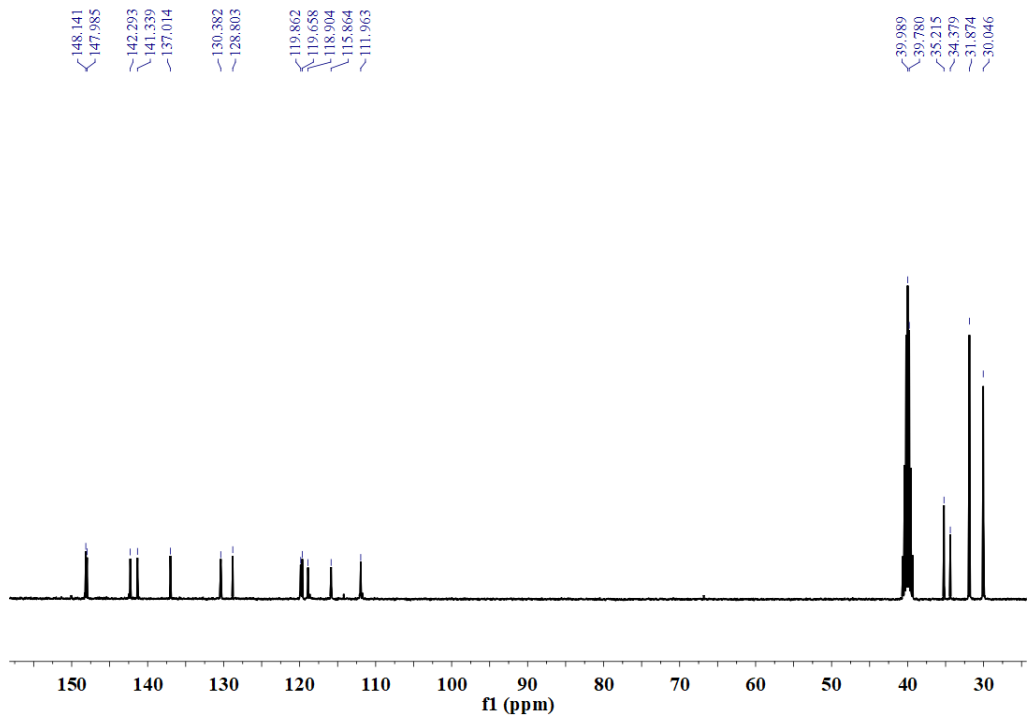

Figure S2. ^{13}C NMR spectrum of **H_4L** (101 MHz, DMSO-d_6, 298 K).

3. Synthesis of 1·CH_3CN and 1·C_6H_6.

1·CH$_3$CN: [Cu(CH$_3$CN)$_4$]ClO$_4$ (163.7 mg, 0.5 mmol) was add to a solution of **H$_4$L** (328.0 mg, 0.5 mmol) and triethylamine (202.0 mg, 2.0 mmol) in acetonitrile (20 mL).The reaction mixture was stirred at ambient temperature for 4 hours in the presence of air to yield dark green suspension. The microcrystalline green solid was collected by filtration and air-dried (305 mg, 80%). Single crystals for X-ray crystallography were grown by slow evaporation of the filtrate. Elemental analysis calcd. (%) for $C_{82}H_{99}Cu_2N_5O_8S_2$: C, 66.82; H, 6.77; N, 4.75. Found: C, 65.85; H, 6.759; N, 3.73. FT-IR of **1·CH$_3$CN** (KBr, 4000-400 cm^{-1}) 3059 (v), 2958 (vs), 2906 (s), 2869 (s), 2249(w), 1581 (m), 1515 (m), 1467 (vs), 1444 (s), 1417 (v), 1361 (s), 1330 (vs), 1301 (s), 1253 (vs), 1203 (s), 1178 (s), 1151 (vs), 1097 (s), 1027 (m), 997 (m), 927 (m), 900 (m), 858 (m), 829 (m), 784 (m), 759 (m), 725 (m), 692 (s), 646 (m), 613 (s), 590 (m), 526 (s), 499 (m), 459(w).

1·C$_6$H$_6$: The **1·CH$_3$CN** (10 mg, 0.0066 mmol) was activated in vacuum at 150 °C for 12 hours. The obtained sample were dissolved in toluene (10 mL), slow evaporation of the solution yield dark-green microcrystal **1·C$_6$H$_6$** (11 mg, 85%).

4. Crystallographic data results.

Table S1. Crystallographic data of **1·CH_3CN** and **1·C_6H_6**.

	1·CH_3CN	**1·C_6H_6**
CCDC number	2070124	2097236
Empirical formula	$C_{80}H_{96}Cu_2N_4O_8S_2$, 2($CH_3CN$)	$C_{80}H_{96}Cu_2N_4O_8S_2$, 6($C_6H_6$)
Formula weight	1514.91	1901.45
Temperature/K	198 (20)	150.01(12)
Crystal system	monoclinic	monoclinic
Space group	$P2_1/c$	C2/c
a/Å	16.0996(2)	28.2254(3)
b/Å	14.3061(2)	14.0966(1)
c/Å	20.0620(3)	30.0105(3)
α/°	90	90
β/°	102.4860(10)	107.9420(10)
γ/°	90	90
Volume/Å^3	4511.44(11)	11359.95(19)
Z	2	4
ρ_{calc} g/cm^3	1.155	1.157
μ/mm^{-1}	1.417	1.235
F(000)	1604.0	4208.0
Crystal size/mm^3	0.020 × 0.015 × 0.015	0.3 × 0.2 × 0.08
Radiation	Cu *K*α (λ = 1.54184)	Cu *K*α (λ = 1.54184)
2Θ range for data collection/°	8.358 to 122.112	6.192 to 145.764
Index ranges	-18 ≤ h ≤ 18, -16 ≤ k ≤ 15, -22 ≤ l ≤ 13	-34 ≤ h ≤ 24, -17 ≤ k ≤ 14, -32 ≤ l ≤ 36
Reflections collected	23127	24074
Independent reflections	6864 [R_{int} = 0.0278, R_{sigma} = 0.0268]	11096 [R_{int} = 0.0228, R_{sigma} = 0.0283]
Data/restraints/parameters	6864/54/521	11096/138/653
Goodness-of-fit on F^2	1.059	1.036
Final R indexes [I>=2σ (I)]	R_1 = 0.0613, wR_2 = 0.1970	R_1 = 0.0660, wR_2 = 0.2142
Final R indexes [all data]	R_1 = 0.0658, wR_2 = 0.2061	R_1 = 0.0708, wR_2 = 0.2221
Largest diff. peak/hole / eÅ^{-3}	1.11/-0.33	1.97/-0.95

$R_1=\sum||F_O|-|F_C||/\sum|F_O|$; $wR_2=[\sum w(F_O^2 - F_C^2)^2 / \sum w(F_O^2)^2]^{1/2}$.

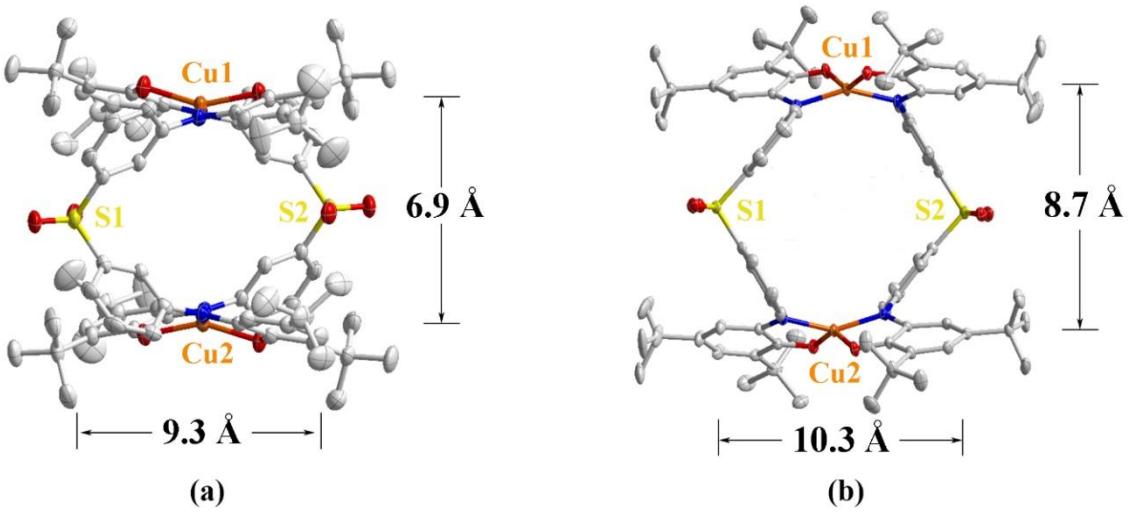

Figure S3. The distance of Cu1-Cu2 and S1-S2 of (a) **1·CH$_3$CN** and (b) **1·C$_6$H$_6$**. The thermal ellipsoids are at the 30% and 40% probability level, respectively. Hydrogen atoms and solvent molecules removed for clarity (C, gray; N, blue; O, red; S, yellow; Cu, orange).

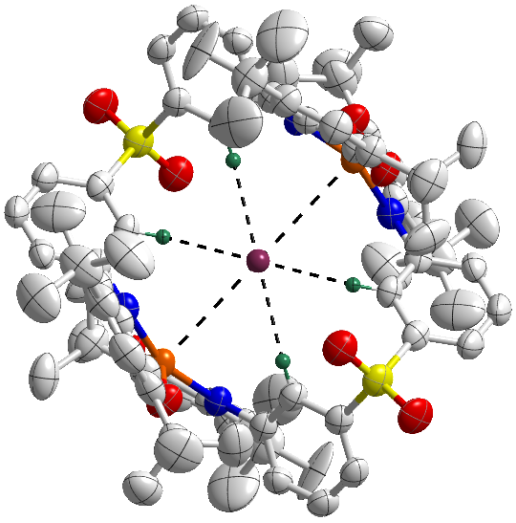

Figure S4. Two open copper sites (orange) and four hydrogen atoms (green) pointing toward the cavity in **1·CH$_3$CN**.

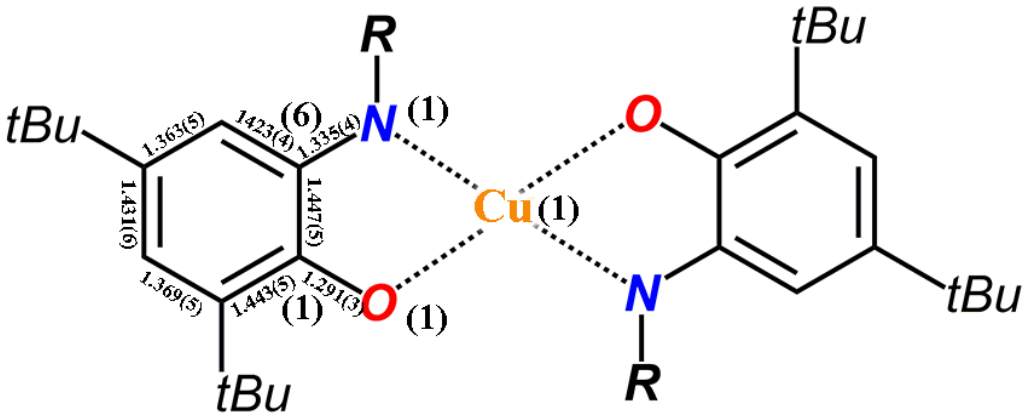

Figure S5. The bond lengths of C1-O1 and C6-N1 are both between the corresponding single-bond (C-N 1.45 and C-O 1.38 Å)[S5] and double-bond values (C=N 1.30 and C=O 1.22 Å)[S6]. The C-C bond lengths in the rings are not equal, which possess a successive short-long-short sequence, followed by three long bond lengths. This feature of distortion is called iminosemiquinonato-type distortion.

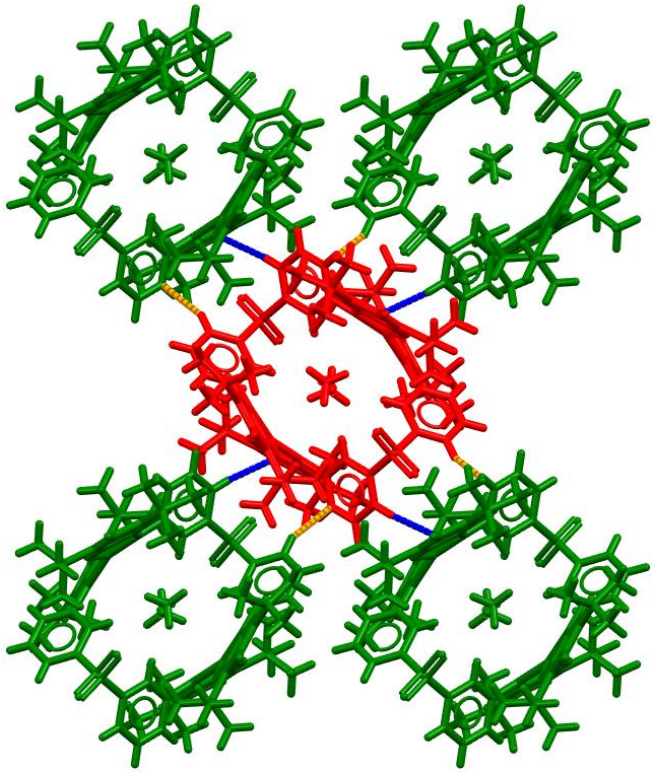

Figure S6. The interaction between metallacycles **1·CH$_3$CN**. C-H···O bond (blue dot line) length is 2.6 Å, and C-H···π bond (orange dot line) length is 2.7 Å.

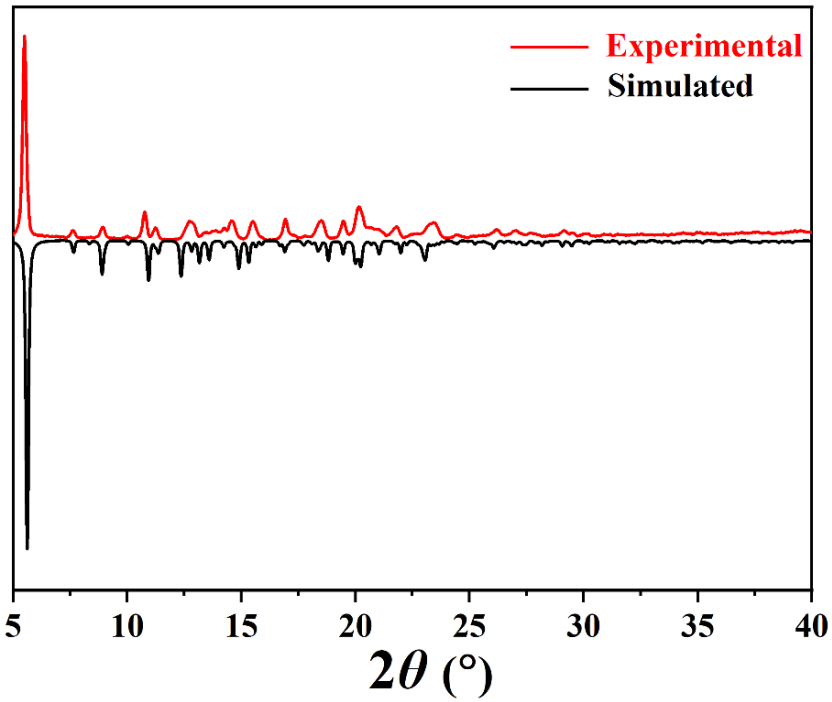

Figure S7. PXRD pattern of **1·CH₃CN**.

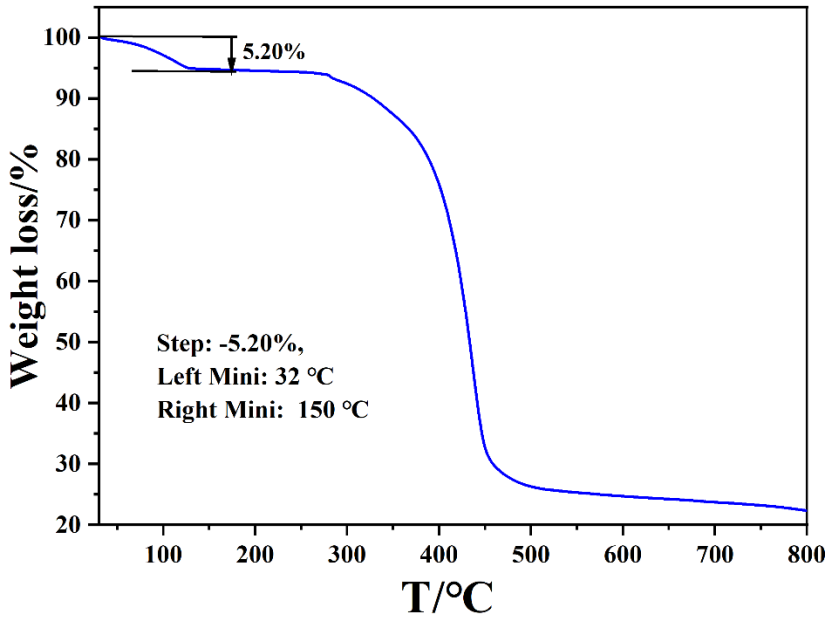

Figure S8. TGA of **1·CH₃CN**.

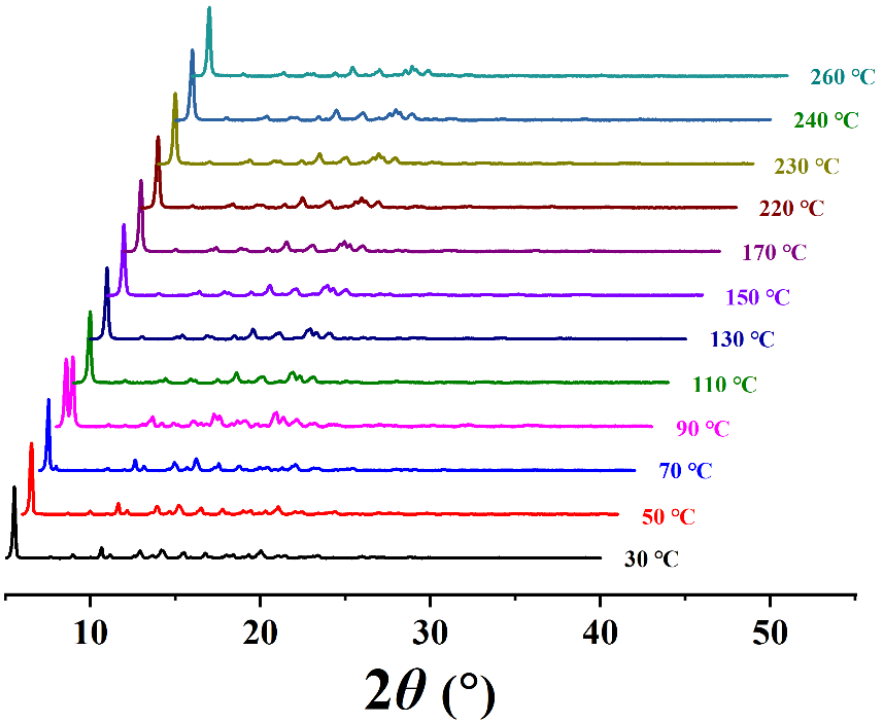

Figure S9. VT-PXRD patterns for **1·CH₃CN**.

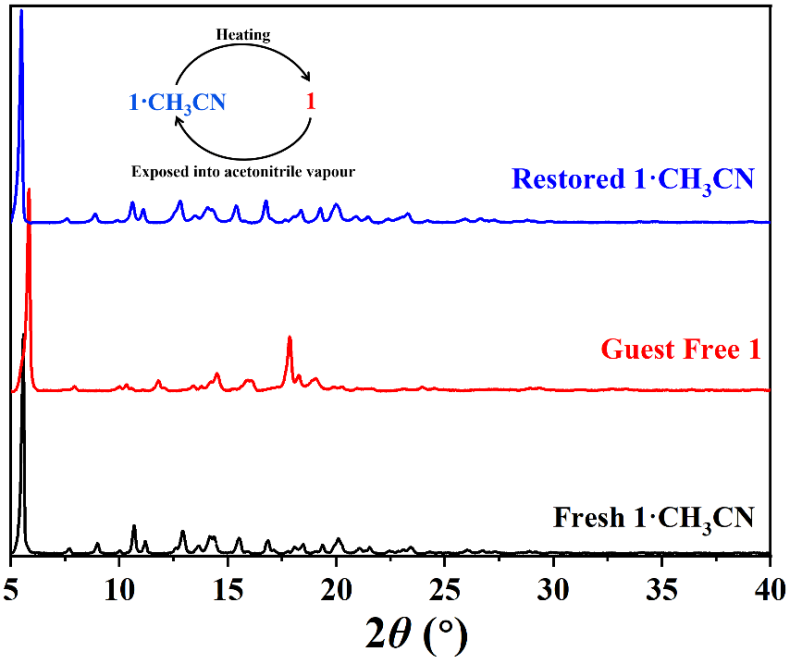

Figure S10. PXRD patterns of reversible transformation between **1·CH₃CN** and **1**.

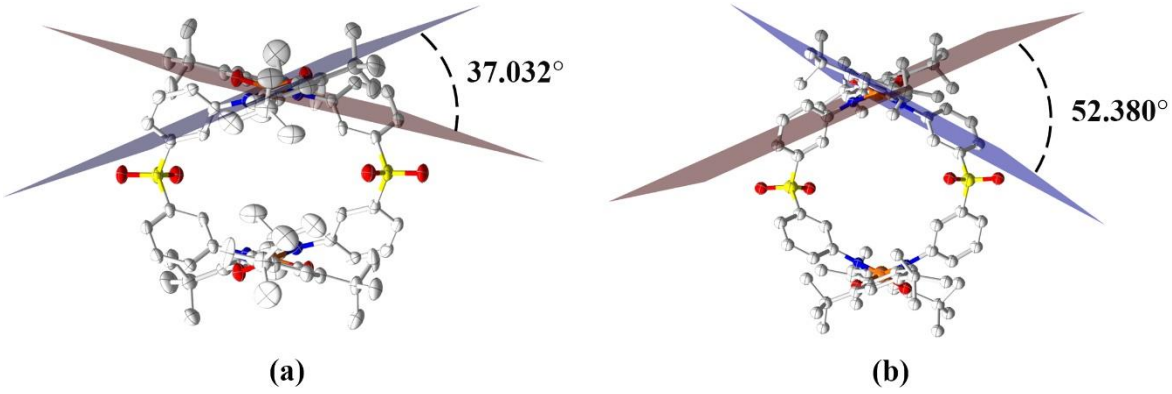

Figure S11. The dihedral angles of the distorted coordinated Cu(II) centers in (a) **1·CH$_3$CN** and (b) **1·C$_6$H$_6$**.

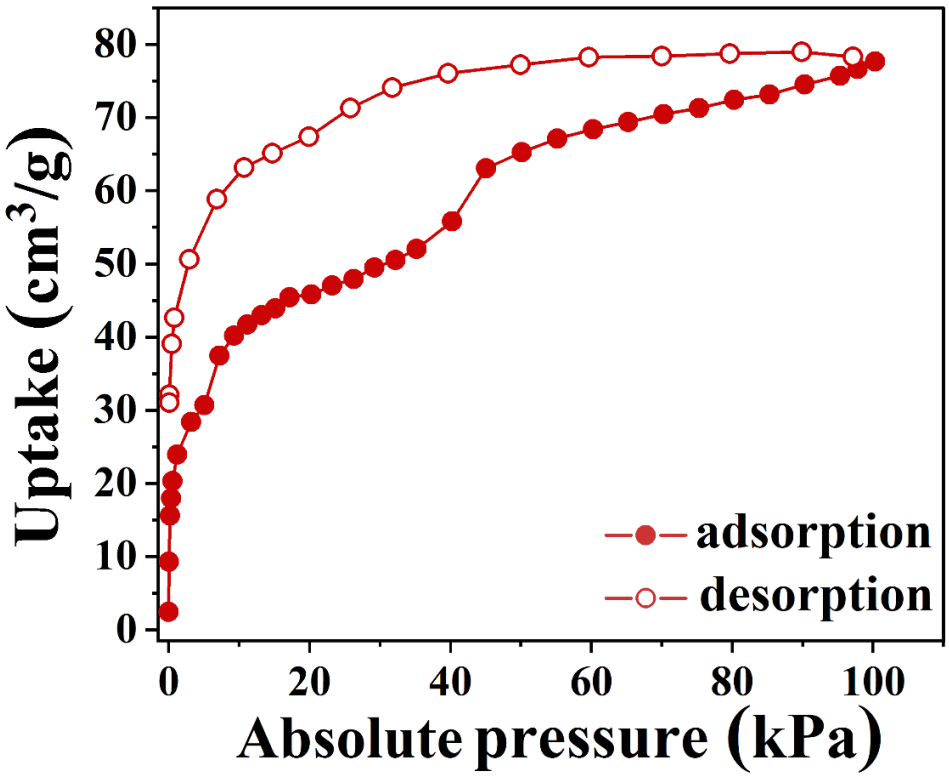

Figure S12. CO_2 adsorption and desorption isotherms (195 K) of **1** obtained from *in situ* adsorption-PXRD measurements (filled circles represent adsorption and empty symbols desorption).

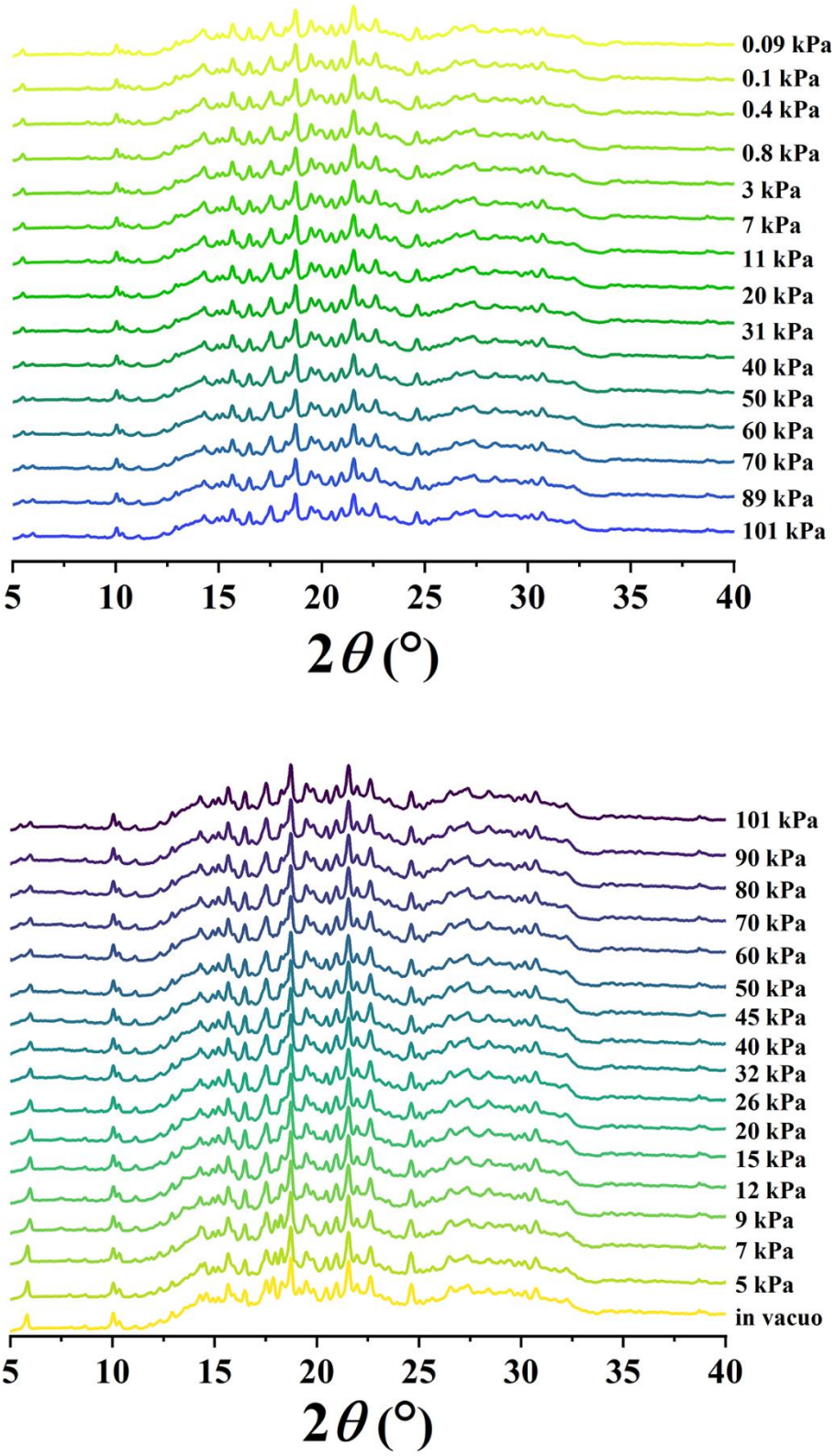

Figure S13. *In situ* PXRD patterns of **1** measured at different equilibrium pressures during adsorption (below) and desorption (up) of CO_2 at 195K.

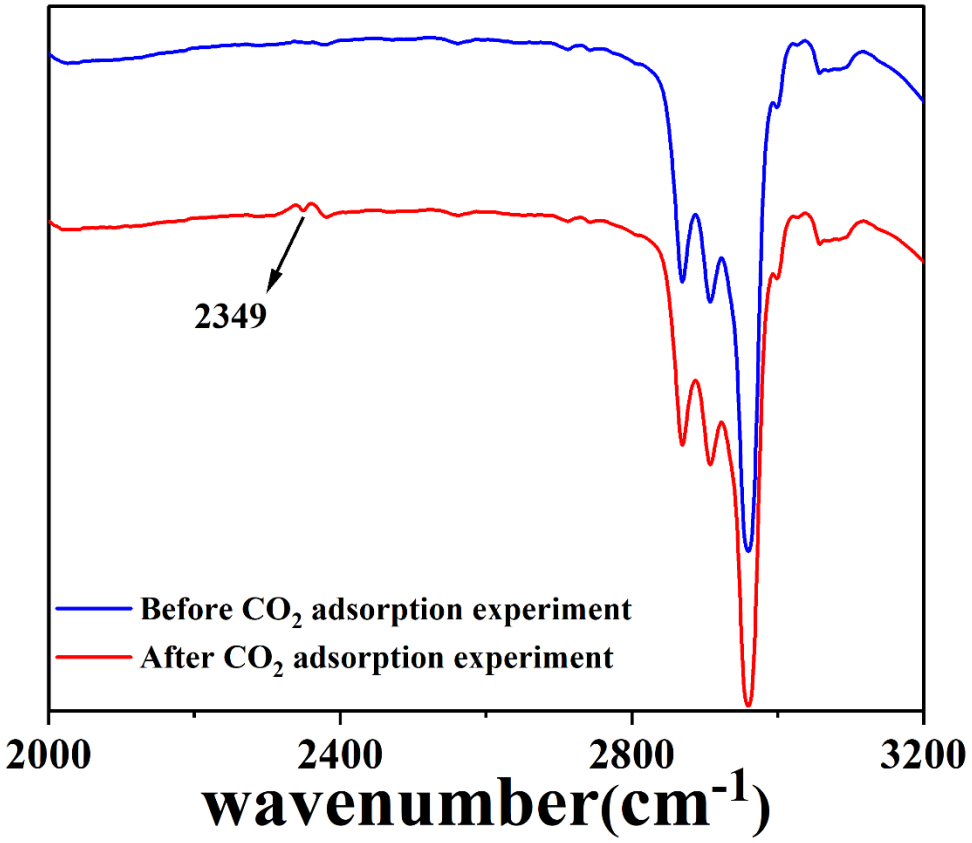

Figure S14. Infrared spectroscopy of **1** before and after CO_2 adsorption experiment.

5. Electrochemical measurements.

Preparation of Working Electrodes. For CV experiments and electrolysis, glassy carbon working electrodes was polished with alumina powder (0.3 and 0.05 μm successively, 60 s per polishing cycle), rinsed with ethanol, and dried in air. 5 mg **1** was dispersed in 950 μL CH_3CN followed by 20 min of sonication. Then, 50 μL Nafion (5 wt%) was added and the complete mixture was further sonicated for 15 min to obtain the final catalytic ink. 10 μL ink was uniformly dropped onto the glassy carbon electrodes (0.196 cm^2) at room temperature (a catalyst loading of 0.25 $mg \cdot cm^{-1}$) and thoroughly dried in air. PXRD patterns of **1** after electrolyzes were carried out using a Toray carbon paper as working electrode. The 50 μL ink was dropped on one face of the carbon paper (area: 1×1 cm^2) and allowed to dry under room temperature prior to use.

Cyclic Voltammetry. Cyclic voltammetry experiments were performed using a CH Instruments, Inc. 660E electrochemical station. Non-catalytic electrochemistry was performed with a three-electrode cell equipped with a glassy carbon working electrode (3.0 mm diameter), a Pt foil counter electrode, and a Pt disk as a pseudo-reference electrode. The electrolyte was 0.1 M $n Bu_4NPF_6$ in CH_2Cl_2 and saturated with N_2 at 298K. Potentials were referenced against Fc/Fc^+ used as an internal standard. For heterogeneous aqueous voltammetry, a H-type cell with a glassy carbon working electrode (5.0 mm diameter), a Pt foil counter electrode and a Ag/AgCl (sat. KCl) reference electrode. The electrolyte used was 0.1 M aq. $KHCO_3$ and saturated with either CO_2 or Ar. No iR was compensation was applied. All the potentials were reported with respect to the RHE, and calculate by the formula, $\boldsymbol{E_{RHE} = E_{Ag/AgCl} + 0.197\ V + 0.0591 \times pH.}$

Preparative scale electrolysis. Preparative scale electrolyzes were performed using a CH Instruments, Inc. 660E electrochemical station. A H-type electrochemical cell was used, Ag/AgCl (sat. KCl) as the reference electrode and graphite as the counter electrode. The electrolyte used was 0.1 M aq. $KHCO_3$ and purged with CO_2 at a rate of 100 sccm for 20 min to obtain the CO_2-saturated solution before electrolysis. During electrochemical measurement, a mass flow controller was used to set the rate of CO_2 at 20 sccm. The potentials without iR compensation and were converted to the RHE as mentioned above.

Flow cell System. Pt foil and Ag/AgCl electrode were used as the counter and reference electrode, respectively. The working electrode was catalyst spray-coated gas diffusion layer (GDL), a catalyst loading was 0.25 $mg \cdot cm^{-1}$. An anion exchange membrane was inserted between the cathode and Pt foil.

Throughout all experiments, 0.1 M $KHCO_3$ electrolyte was flowed in the cathode and anode chambers separately at 25 mL·min^{-1} with a peristaltic pump, while CO_2 gas was flowed behind the GDL with a flow rate of 20 sccm using a mass flow controller. All the electrolyzer components have verified to be chemically resistant to all the reactants and products under the CO_2 reduction potentials prior to experiments.

Product analysis. Gas products were analyzed by an on-line GC (Agilent C7890) equipped with a 30 m long Agilent 115-3532PT column. N_2 as carrier gas. TCD, FID A and FID B were used for the quantification of CO, hydrocarbon compounds (CH_4, C_2H_2) and H_2, respectively. The volume concentration of certain gas product was calculated by gas chromatography peak areas based on standard curves of pure samples. The liquid products were detected by ^{1}H NMR.

The Faradaic Efficiency of gas products were calculated by the formula:

$$\boldsymbol{FE}(\%) = \frac{\boldsymbol{PV}}{\boldsymbol{RT}} \times \frac{\boldsymbol{vNF} \times \boldsymbol{10^{-6}}\,(\boldsymbol{m^3/mL})}{\boldsymbol{I} \times \boldsymbol{60}\ \ (\boldsymbol{s/min})} \times \boldsymbol{100}\%$$

v: volume concentration of gas product in the exhaust gas from the electrochemical cell (GC data);

V: gas flow rate, 20 mL·min^{-1};

I: total steady-state cell current, mA;

P: the measured pressure value, 109025.8 Pa;

R: universal gas constant, 8.314 J·mol^{-1}·K^{-1};

T: test temperature, 303.67 K;

N: the electron transfer number for product formation;

F: Faradaic constant, 96485 C·mol^{-1}.

The turnover frequency (TOF, s^{-1}) was defined as the mole of reduction product generated per electrocatalytic active site per unit time. The TOF was calculated by the formula:

$$\boldsymbol{TOF}(\boldsymbol{h^{-1}}) = \frac{\boldsymbol{j_{total}} \times \boldsymbol{FE_{average}}}{\boldsymbol{N} \times \boldsymbol{F} \times \boldsymbol{n_{cat.}}} \times \boldsymbol{3600}(\boldsymbol{s/h})$$

$\boldsymbol{j_{total}}$**:** the total density at certain potential, mA·cm^{-2};

FE: the average Faradaic efficiency of certain product, %;

N: the electron transfer number for product formation;

F: Faradaic constant, 96485 C·mol^{-1};

n_{cat}: the moles of catalyst employed in electrolysis, mol.

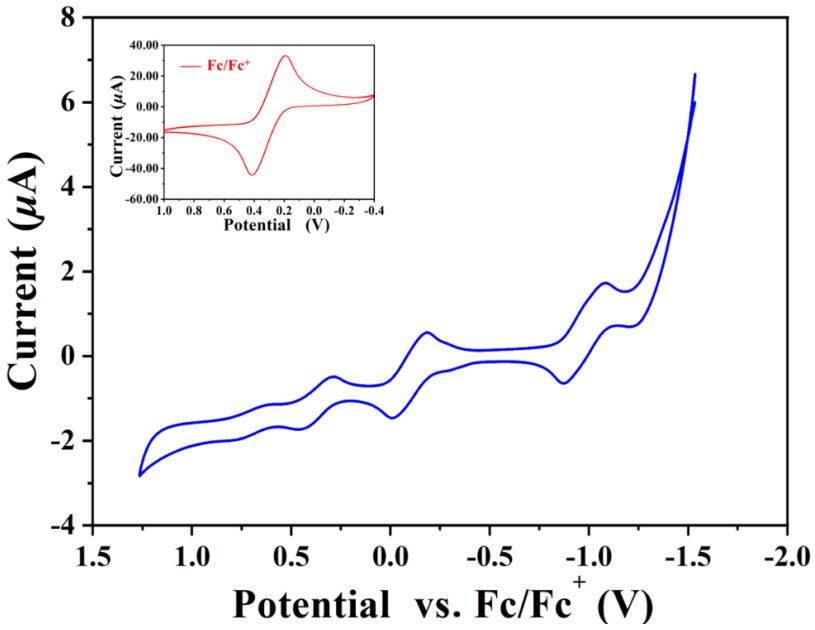

Figure S15. CV of 3.84×10^{-2} mM **1** in CH_2Cl_2 containing 0.1 M nBu_4NPF_6 under N_2 at a scan rate of 20 mV/s.

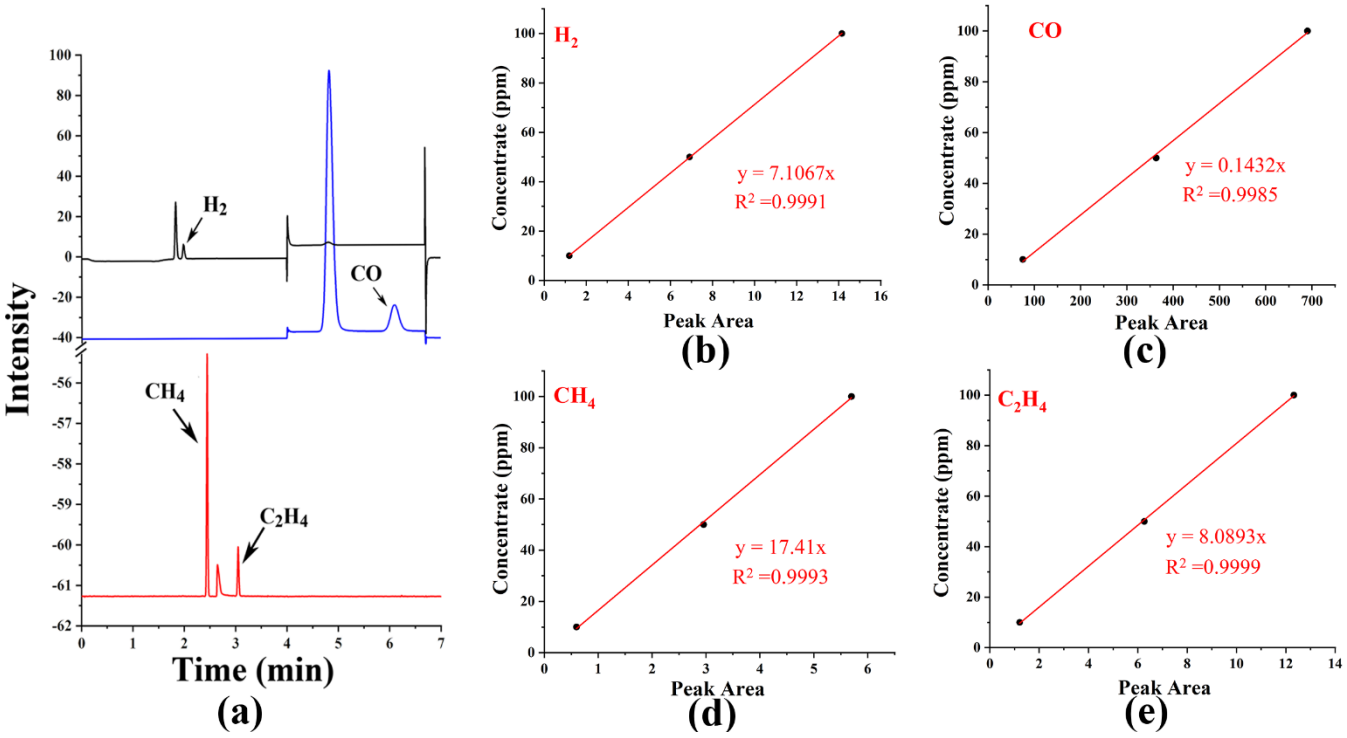

Figure S16. (a) GC profiles for electrocatalytic reaction of **1**. (b)-(e) Calibration curves of H_2, CO, CH_4 and C_2H_4.

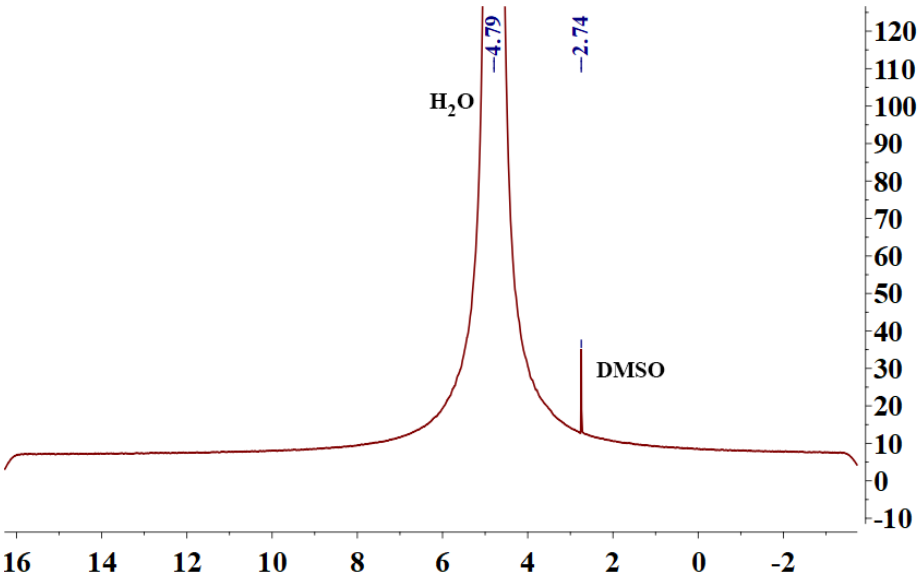

Figure S17. The ^{1}H NMR spectrum of the liquid phase after electrocatalysis. DMSO was used as an internal standard.

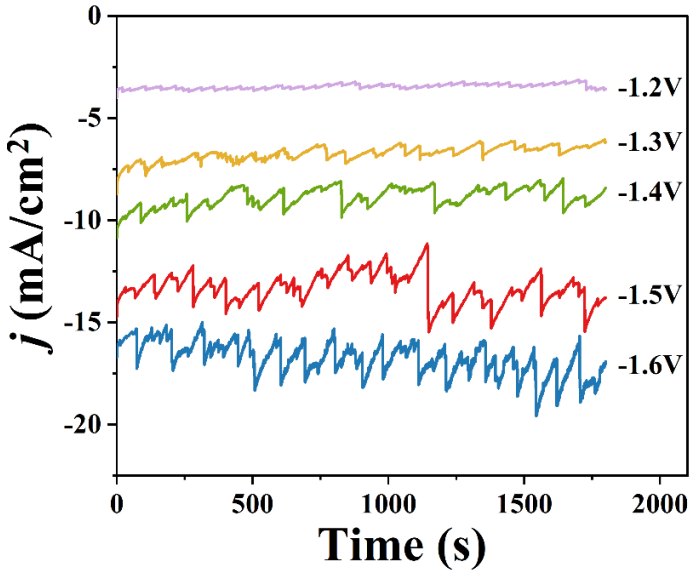

Figure S18. Variation of the current density as a function of the electrolysis potential.

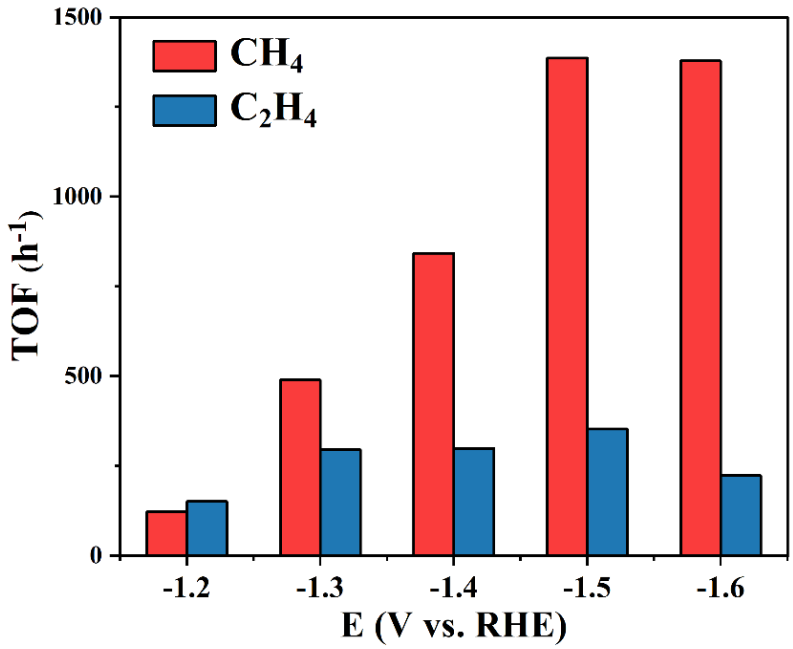

Figure S19. The turnover frequencies (TOFs) for CH_4 and C_2H_4 at various potentials.

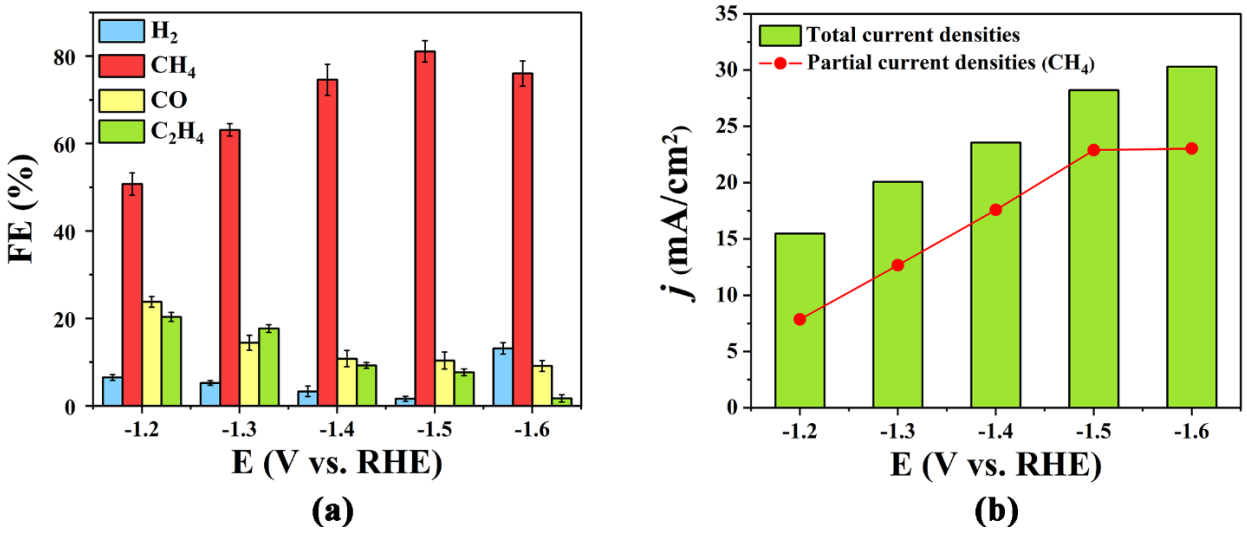

Figure S20. CO_2 reduction Faradaic efficiency (a) and partial current densities at selected potentials (b) in a flow cell device.

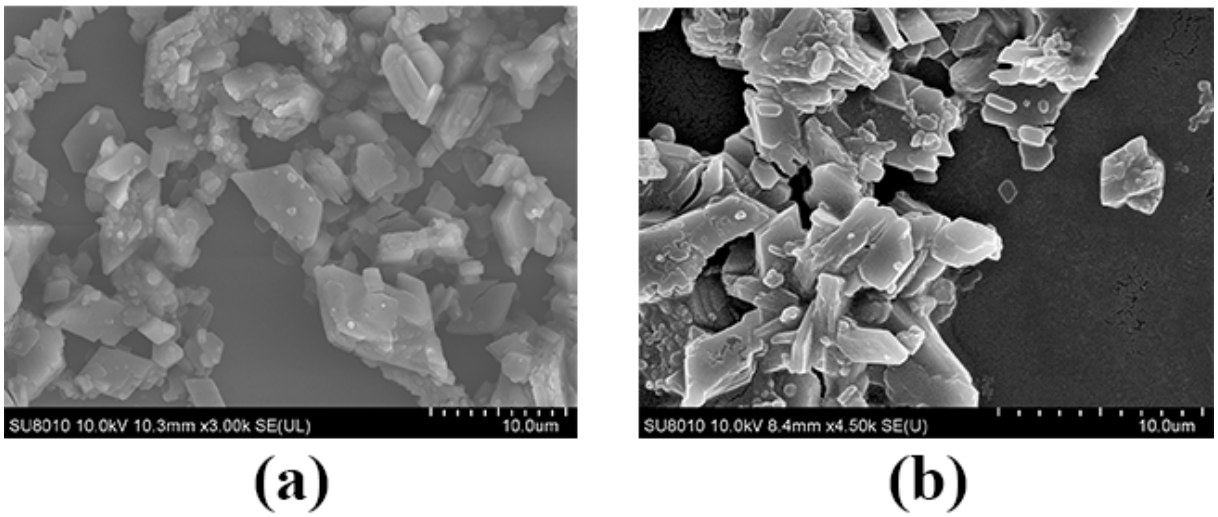

Figure S21. SEM images of the catalyst electrode (a) before and (b) after electrocatalysis.

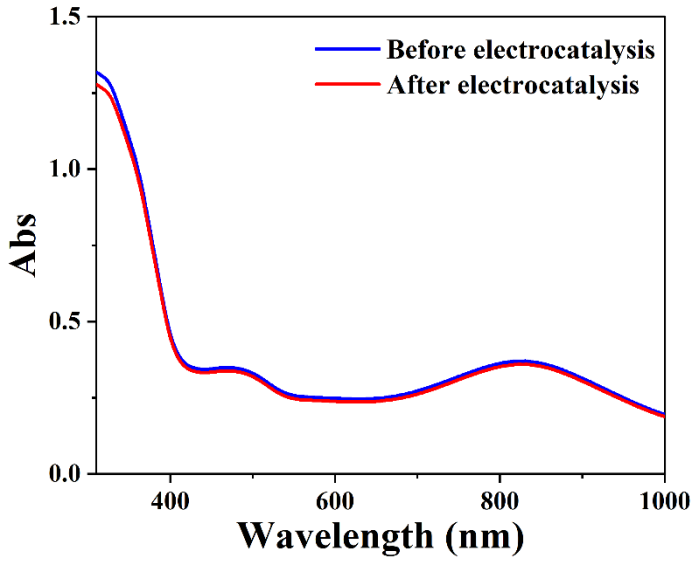

Figure S22. UV-Vis spectra before and after electrocatalysis.

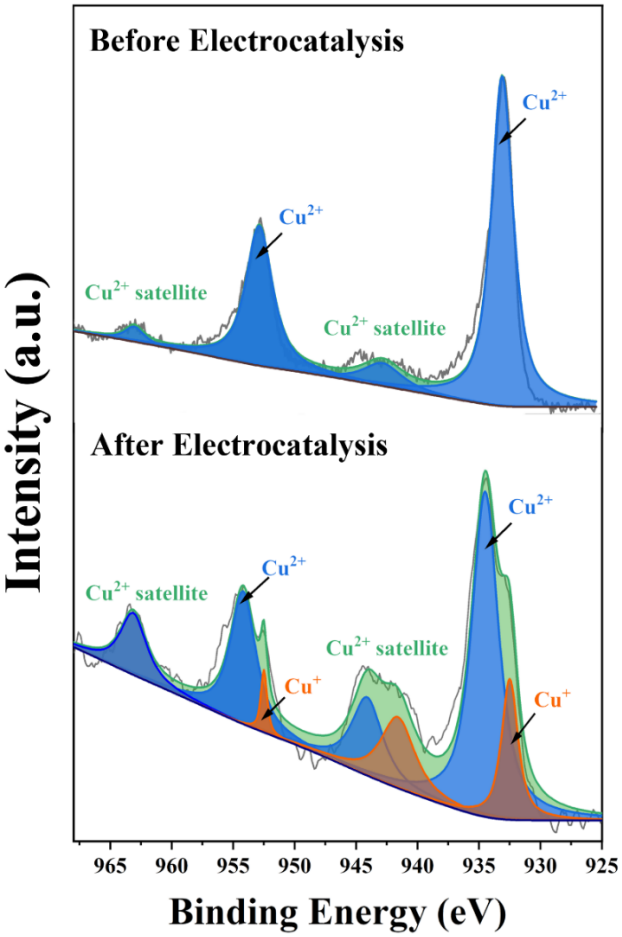

Figure S23. Cu 2*p* XPS spectra before and after electrocatalysis.

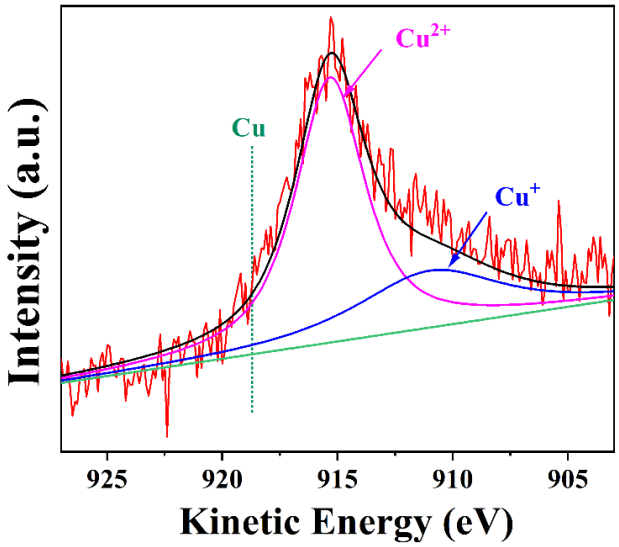

Figure S24. Cu LMM Auger spectra of the catalyst after electrocatalysis.

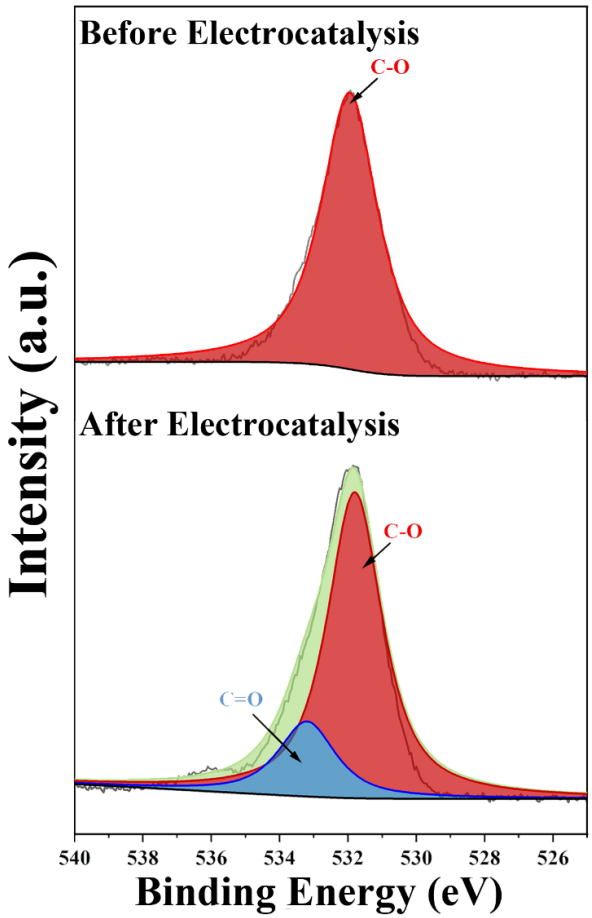

Figure S25. O 1*s* XPS spectra before and after electrocatalysis.

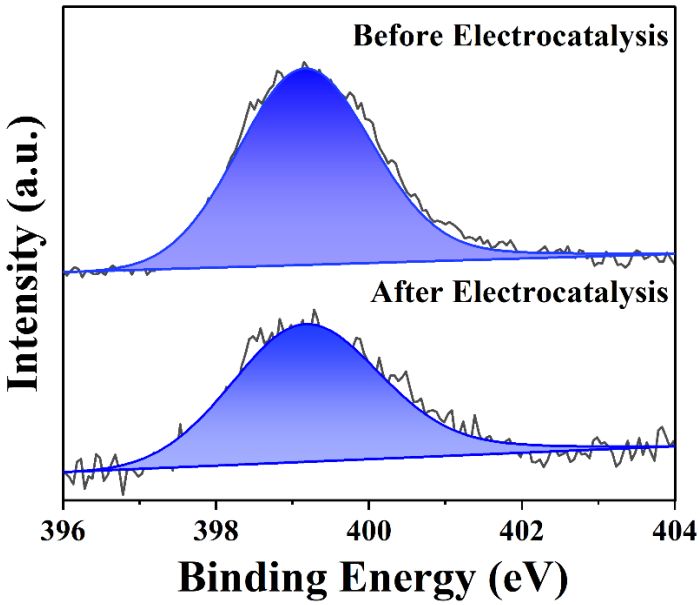

Figure S26. N 1*s* XPS spectra before and after electrocatalysis.

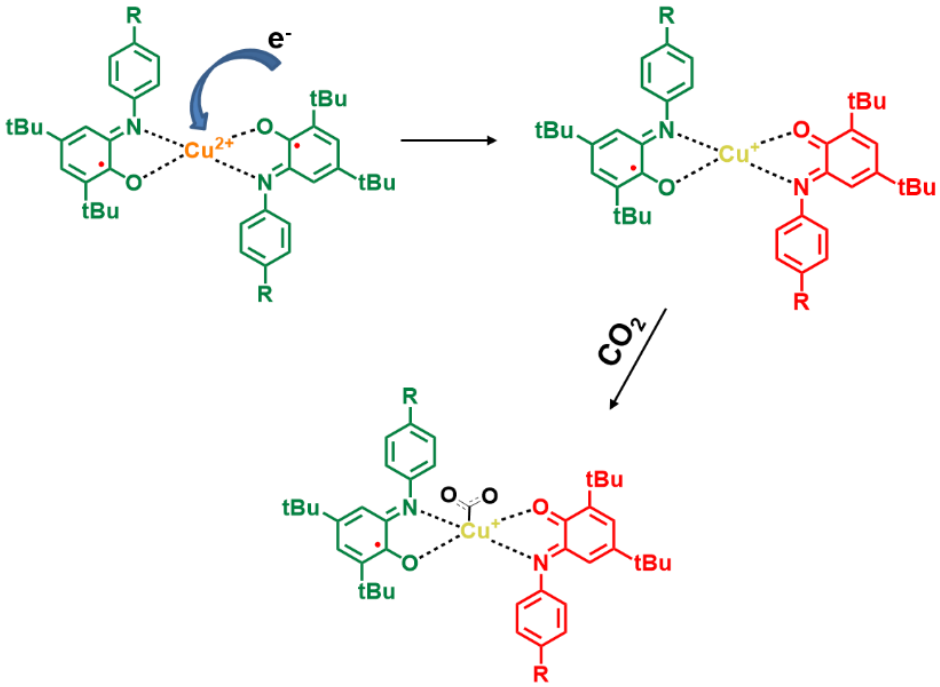

Figure S27. Illustration of the conversion from Cu(II) to Cu(I) ions and the binding with CO_2 during the electrocatalysis.

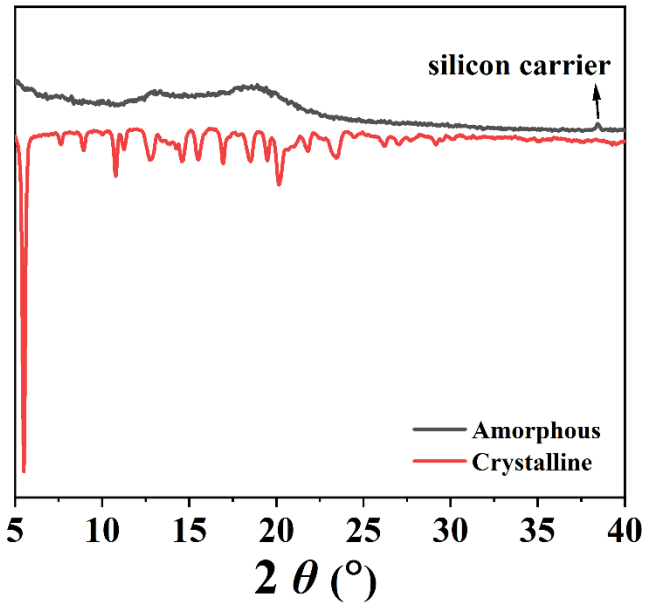

Figure S28. The PXRD patterns of amorphous and crystalline powders.

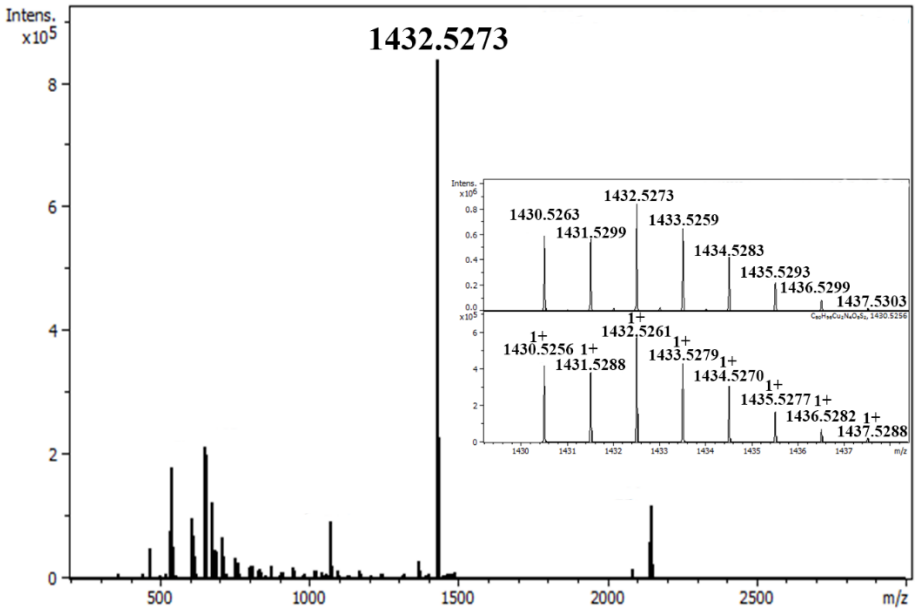

Figure S29. HR-ESI (m/z) of amorphous powder: calcd. for [Cu_2L_2-H]$^+$, 1432.88. Found: [Cu_2L_2-H]$^+$, 1432.5273.

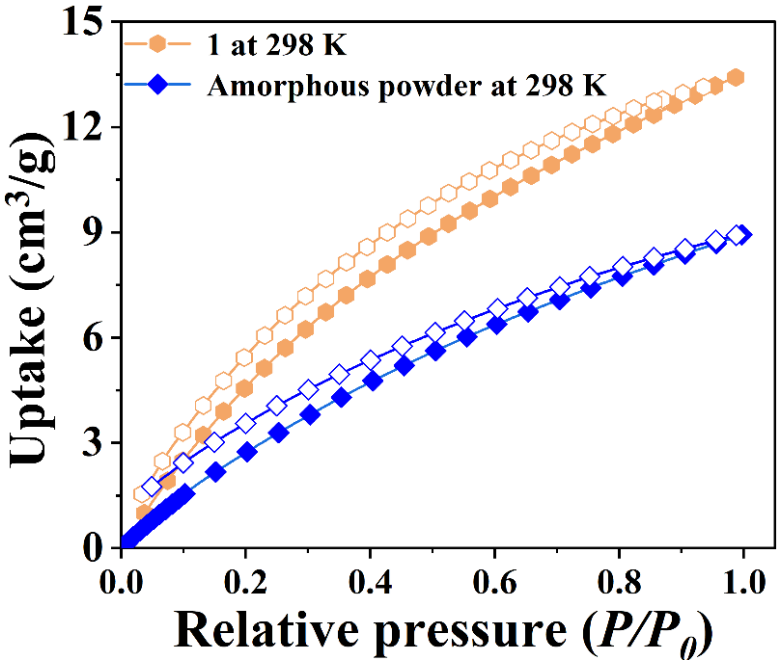

Figure S30. CO_2 isotherms of **1** and amorphous powder at 298 K (solid symbols: adsorption, open symbols: desorption).

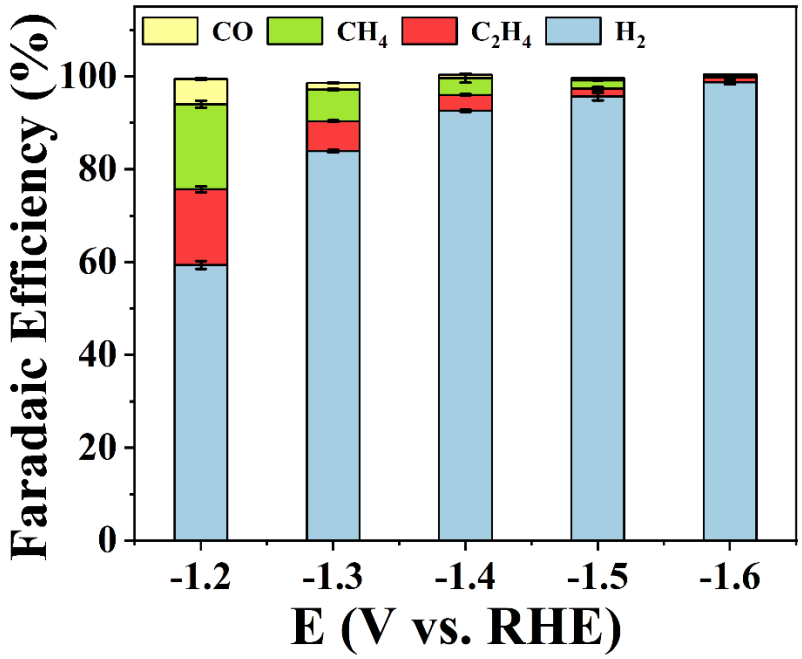

Figure S31. CO_2 reduction Faradaic efficiency of amorphous powder.

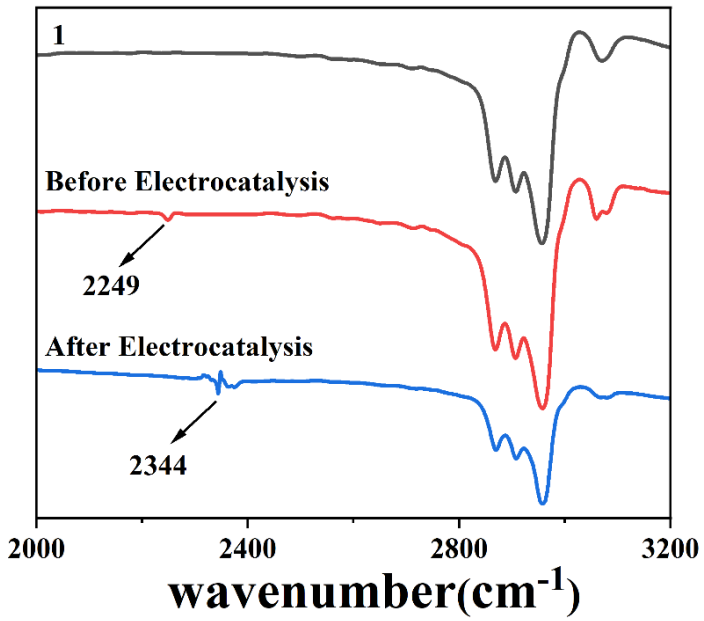

Figure S32. IR spectra of **1** before and after electrocatalysis. (**1**: activated sample. Before Electrocatalysis: the sample collected from catalytic ink before electrochemical treatment.)

Table S2. Comparison of the CO_2RR performance with other electrocatalysts for CO_2-to-CH_4 reported previously.

Material	FE(%)				Electrolyte	E vs. RHE (V)	Ref.
	H_2	CO	CH_4	C_2H_4			
1	**13**	**4**	**70**	**13**	**0.1 M $KHCO_3$**	**-1.5**	**This work**
1 (flow-cell)	**1.6**	**10**	**81**	**7**	**0.1 M $KHCO_3$**	**-1.5**	**This work**
Cu Porphyrin	--	10	27	--	0.5 M $KHCO_3$	-0.976	S7
Cu Phthalocyanine + CNT	34	--	66	--	0.5 M $KHCO_3$	-1.06	S8
Cu Phthalocyanine	25	5	5	25	0.5 M KCl	-1.7 (Ag/AgCl)	S9
Co Protoporphyrin[1]	--	6.7	2.3	--	0.1 M $KClO_4$	-0.8	S10
Cu	42.8	20.2	4.7	12.4	0.1 M KCO_3	-1.1	S11
Cu_2O@CuHHTP	--	--	73	--	0.1 M KCl / 0.1 M $KHCO_3$	-1.4	S12
HKUST-1 + CNT	60	5	25	--	0.5 M $KHCO_3$	-1.06	S8
Cu dimer distorted HKUST-1	7	24	0.4	45	1 M KOH	-1.07	S13
HATNA-Cu-MOF	16	--	78	--	0.1 M $KHCO_3$	-1.5	S14
Cu Carbon-dots-based SAC	--	--	78	--	0.5 M $KHCO_3$	-1.44	S15
Porphyrin-based monoatomic layers	16.4	5.85	11.51	0	0.1 M $KHCO_3$	-0.7	S16
Cu-TDPP-NS (flow-cell)	--	--	70	--	0.5 M PBS	-1.6	S17

[1] $p(CO_2)$= 10 atm.

6. Computational methods.

The simulations were carried out by quantum chemistry package Gaussian16 based on density functional theory (DFT).[S18] All optimized geometries were performed B3LYP* method [S19] and 6-311G basis set,[S20] and there is no imaginary frequency of these structures. All structures were optimized until energy difference less than 1×10^{-12} Hartree, and the force of atom smaller than 0.00045 Hartree/Bohr. The vibration frequencies of systems were calculation by second derivative of Hamiltonian, i.e. the Hessian matrix. The Gibbs free energy was calculated by $\Delta \boldsymbol{G} = \Delta \boldsymbol{E} + \Delta \boldsymbol{E_{ZPE}} - \boldsymbol{T}\Delta \boldsymbol{S}$, where $\boldsymbol{T}$ is the temperature in Kelvin, $\boldsymbol{\Delta S}$ is the entropy difference, $\boldsymbol{\Delta E}$ is the total energy difference and $\boldsymbol{\Delta E_{ZPE}}$ is the zero-point energy difference.[S21,S22] The theoretical limiting potential could be obtained by $\boldsymbol{U_L} = -\Delta \boldsymbol{G_{max}}/\boldsymbol{e}$, where $\boldsymbol{e}$ is the elementary charge, and the step with the $\boldsymbol{\Delta G_{max}}$ is the potential determining step.

Table S3. Free energy change (eV) for each elementary step during CO_2RR.

Reaction steps	$\boldsymbol{\Delta G}$ (eV)
$* + CO_2 + [H^+ + e^-] \rightarrow *COOH$	0.60
$*COOH + [H^+ + e^-] \rightarrow *CO + H_2O$	-0.92
$*CO + [H^+ + e^-] \rightarrow *COH$	1.69
$*COH + [H^+ + e^-] \rightarrow *CHOH$	-0.48
$*CHOH + [H^+ + e^-] \rightarrow *CH + H_2O$	0.04
$*CH + [H^+ + e^-] \rightarrow *CH_2$	-0.90
$*CH_2 + [H^+ + e^-] \rightarrow *CH_3$	-1.19
$*CH_3 + [H^+ + e^-] \rightarrow * + CH_4$	-0.33

References

S1. L. Czepirski, J. JagiełŁo. Virial-type thermal equation of gas-solid adsorption. *J. Chem. Eng. Sci.* **1989**, *44*, 797-801.

S2. G. M. Sheldrick. SADABS: *Program for Empirical Absorption Correction of Area Detector Data*; University of Göttingen: Göttingen, Germany, **1996**.

S3. G. M. Sheldrick. SHELXL 2014. *Acta Crystallogr., Sect. C: Struct. Chem*. **2015**, *71*, 3-8.

S4. D. A. Safin; K. Robeynsa; Y. Garcia. Solid-state thermo- and photochromism in N,N'-bis(5-X-salicylidene)diamines (X = H, Br). *RSC Adv.* **2012**, *2*, 11379-11388.

S5. C. Mukherjee, T. Weyhermüller, E. Bothe, P. Chaudhuri. Oxidation of an o-iminobenzosemiquinone radical ligand by molecular bromine: structural, spectroscopic, and reactivity studies of a copper(II) o-iminobenzoquinone complex. *Inorg. Chem.* **2008**, *47*, 2740-2746.

S6. S. Ghoraia, C. Mukherjee. Effect of ligand substituent on the reactivity of Ni(II) complexes towards oxygen. *Dalton Trans.* **2014**, *43*, 394-397.

S7. Z. Weng, J. Jiang, Y. Wu, Z. Wu, X. Guo, K. L. Materna, W. Liu, V. S. Batista, G. W. Brudvig, H. Wang. Electrochemical CO_2 Reduction to hydrocarbons on a heterogeneous molecular Cu catalyst in aqueous solution, *J. Am. Chem. Soc.* **2016**, *138*, 8076-8079.

S8. Z. Weng, Y. Wu, M. Wang, J. Jiang, K. Yang, S. Huo, X.-F. Wang, Q. Ma, G. W. Brudvig, V. S. Batista, Y. Liang, Z. Feng, H. Wang. Active sites of copper-complex catalytic materials for electrochemical carbon dioxide reduction, *Nat. Commun.* **2018**, *9*, 415.

S9. S. Kusama, T. Saito, H. Hashiba, A. Sakai, S. Yotsuhashi. Crystalline copper(II) phthalocyanine catalysts for electrochemical reduction of carbon dioxide in aqueous media, *ACS Catal.* **2017**, *7*, 8382-8385.

S10. J. Shen, R. Kortlever, R. Kas, Y. Y. Birdja, O. Diaz-Morales, Y. Kwon1, I. Ledezma-Yanez1, K. J. P. Schouten, G. Mul, M. T.M. Koper. Electrocatalytic reduction of carbon dioxide to carbon monoxide and methane at an immobilized cobalt protoporphyrin, *Nat. Commun*. **2015**, *6*, 8177.

S11. Z. Han, R. Kortlever, H. Chen, J. C. Peters, T. Agapie. CO_2 reduction selective for C ≥ 2 products on polycrystalline copper with N-substituted pyridinium additives, *ACS Cent. Sci.* **2017**, *3*, 853-859.

S12. J.-D. Yi, R. Xie, Z.-L. Xie, G.-L. Chai, T.-F. Liu, R.-P. Chen, Y.-B. Huang, R. Cao. Highly selective CO_2 electroreduction to CH_4 by in situ generated Cu_2O single-type sites on a conductive MOF: stabilizing key intermediates with hydrogen bonding, *Angew. Chem., Int. Ed*. **2020**, *59*, 23641-23648.

S13. D.-H. Nam, O. S. Bushuyev, J. Li, P. D. Luna, A. Seifitokaldani, C.-T. Dinh, F. P. G. Arquer, Y. Wang, Z. Liang, A. H. Proppe, C. S. Tan, P. Todorović, O. Shekhah, C. M. Gabardo, J. W. Jo, J. Choi, M.-J. Choi, S.-W. Baek, J. Kim, D. Sinton, S. O. Kelley, M. Eddaoudi, E. H. Sargent. Metal-organic frameworks mediate Cu coordination for selective CO_2 electroreduction, *J. Am. Chem. Soc.* **2018**, *140*, 11378-11386.

S14. Y. Liu, S. Li, L. Dai, J. Li, J. Lv, Z. Zhu, A. Yin, P. Li, B. Wang. The Synthesis of hexaazatrinaphthylene-based 2D conjugated copper metal-organic framework for highly selective and stable electroreduction of CO_2 to methane, *Angew. Chem., Int. Ed*. **2021**, *60*, 16409-16415.

S15. Y. Cai, J. Fu, Y. Zhou, Y.-C. Chang, Q. Min, J.-J. Zhu, Y. Lin, W. Zhu. Insights on forming N,O-coordinated Cu singleatom catalysts for electrochemical reduction CO_2 to methane, *Nat. Commun.* **2021**, *12*, 586.

S16. D. Yang, S. Zuo, H. Yang, Y. Zhou, X. Wang. Freestanding millimeter-scale porphyrin-based monoatomic layers with 0.28 nm thickness for CO_2 electrocatalysis, *Angew. Chem., Int. Ed*. **2020**, *59*, 18954-18959.

S17. Y.-R. Wang, M. Liu, G.-K. Gao, Y.-L. Yang, R.-X. Yang, H.-M. Ding, Y. Chen, S.-L. Li, Y.-Q. Lan, Implanting numerous hydrogen-bonding networks in a Cu-porphyrin-based nanosheet to boost CH_4 selectivity in neutral-media CO_2 electroreduction, *Angew. Chem., Int. Ed.* **2021**, *60*, 21952-21958.

S18. M. J. Frisch, G. W. Trucks, H. B. Schlegel, G. E. Scuseria, M. A. Robb, J. R. Cheeseman, G. Scalmani, V. Barone, G. A. Petersson, H. Nakatsuji, X. Li, M. Caricato, A. V. Marenich, J. Bloino, B. G. Janesko, R. Gomperts, B. Mennucci, H. P. Hratchian, J. V. Ortiz, A. F. Izmaylov, J. L. Sonnenberg, D. Williams-Young, F. Ding, F. Lipparini, F. Egidi, J. Goings, B. Peng, A. Petrone, T. Henderson, D. Ranasinghe, V. G. Zakrzewski, J. Gao, N. Rega, G. Zheng, W. Liang, M. Hada, M. Ehara, K. Toyota, R. Fukuda, J. Hasegawa, M. Ishida, T. Nakajima, Y. Honda, O. Kitao, H. Nakai, T. Vreven, K. Throssell, J. A. Montgomery, Jr., J. E. Peralta, F. Ogliaro, M. J. Bearpark, J. J. Heyd, E. N. Brothers, K. N. Kudin, V. N. Staroverov, T. A. Keith, R. Kobayashi, J. Normand, K. Raghavachari, A. P. Rendell, J. C. Burant, S. S. Iyengar, J. Tomasi, M. Cossi, J. M. Millam, M. Klene, C. Adamo, R. Cammi, J. W. Ochterski, R. L. Martin, K. Morokuma, O. Farkas, J. B. Foresman, and D. J. Fox, Gaussian, Inc., Wallingford CT, **2019**.

S19. A. D. Becke, Density-functional thermochemistry. III. The role of exact exchange. *J. Chem. Phys.* **1993**, *98*, 5648-5652.

S20. B. P. Pritchard, D.Altarawy, B. Didier, T. D. Gibson, T. L. Windus. A new basis set exchange: an open, up-to-date resource for the molecular sciences community. *J. Chem. Inf. Model.* **2019**, *59*, 4814-4820.

S21. A. A. Peterson, F. Abild-Pedersen, F. Studt, J. Rossmeisl, J. K. Nørskov. How copper catalyzes the electroreduction of carbon dioxide into hydrocarbon fuels. *Energy Environ. Sci.* **2010**, *3*, 1311-1315.

S22. T. Liu, Q. Wang, G. Wang, X. Bao. Electrochemical CO_2 reduction on graphdiyne: a DFT study. *Green Chem.* **2021**, *23*, 1212-1219.